

NASA TECHNICAL NOTE

NASA TN D-2383

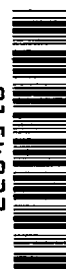


NASA TN D-2383

C.1

LOAN COPY: RETURN  
AFWL (WLIL-2)  
KIRTLAND AFB, N ME

0154933



TECH LIBRARY KAFB, NM

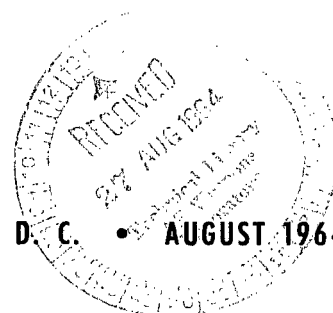
# HEAT-TRANSFER RATES AND ABLATION ON A BLUNTED CYLINDER-FLARE CONFIGURATION IN FREE FLIGHT UP TO A MACH NUMBER OF 8.98

*by Clyde W. Winters*

*Langley Research Center*

*Langley Station, Hampton, Va.*

NATIONAL AERONAUTICS AND SPACE ADMINISTRATION • WASHINGTON, D. C. • AUGUST 1964





HEAT-TRANSFER RATES AND ABLATION ON A  
BLUNTED CYLINDER-FLARE CONFIGURATION IN FREE FLIGHT  
UP TO A MACH NUMBER OF 8.98

By Clyde W. Winters

Langley Research Center  
Langley Station, Hampton, Va.

NATIONAL AERONAUTICS AND SPACE ADMINISTRATION

---

For sale by the Office of Technical Services, Department of Commerce,  
Washington, D.C. 20230 -- Price \$0.75

HEAT-TRANSFER RATES AND ABLATION ON A  
BLUNTED CYLINDER-FLARE CONFIGURATION IN FREE FLIGHT

UP TO A MACH NUMBER OF 8.98

By Clyde W. Winters  
Langley Research Center

SUMMARY

A three-stage rocket-propelled vehicle system was flown to a maximum Mach number of 8.98 to determine the ablation characteristics of several ablative materials and the heating rates over various sections of a blunted cylinder-flare configuration. Continuous in-flight measurements were made over the teflon nose cone in which ablation sensors, developed by the National Aeronautics and Space Administration, were installed. The ablated-length measurements were in close agreement with analytical predictions. In-flight temperature measurements were also made over the inner surface of uncoated inconel sections (serving as calorimeters) behind the nose cone as well as over the inner surface of sections coated with several ablative materials. These measurements were used to calculate the heating rates for the analysis of the ablative materials.

INTRODUCTION

The realization that the ablation process can be used as a powerful heat absorption mechanism during hypersonic reentry has led to the development of many different ablative materials (ref. 1). Frequently, these materials have been tested in various test facilities for the purpose of obtaining their ablation properties and characteristics (ref. 2). Furthermore, test results have sometimes been applied to flight conditions without regard to the difference between the flight environment and the ground test environment. However, in many instances the interpretation of the test results in terms of performance has been nebulous because of insufficient knowledge of the important simulation parameters (e.g., ablation temperature and effective heat of ablation) for the different ablating materials.

Some of the early studies in this field which examined ablative materials both theoretically and experimentally are noted in reference 3. These studies have all shown that ablation involves a number of complex mechanisms which require knowledge of material properties in various physical states. The data obtained from these studies were combined in an analytical investigation, reference 3, whereby expressions were developed to predict the ablation rates of

ablative materials. In order to verify these analytical expressions a flight research program involving three test vehicles, utilizing NASA developed ablation sensors in the nose cones, was initiated at the Langley Research Center. These test vehicles have been flown successfully and the results of the first two investigations are reported in references 4 and 5.

The purpose of this paper is to present the results and analysis of the third test vehicle, which was flown to a maximum Mach number of 8.98 by using a three-stage solid-propellant launch-vehicle system. The main objective of the investigation was to measure the in-flight ablation rates over the blunted teflon nose cone, and to compare these results with the results predicted by the analytical method of Rashis and Hopko (ref. 3). Secondary objectives were to make similar comparisons between theoretical and experimental results of the ablation rates on the cylindrical section behind the nose cone and the stabilizing flare of the free-flight model. Each of these sections had one-half of their respective surface areas covered with subliming types of ablative materials. Ablation data obtained over the cylinder and flare segments were compared with data computed by means of the analysis developed in reference 6, which utilized a computer program.

## SYMBOLS

$c_p$	specific heat at constant pressure, Btu/lb-°F
$c_{p,c}$	specific heat of teflon vapor at wall temperature, Btu/lb-°F
$c_{p,l}$	specific heat of air at local temperature, Btu/lb-°F
$H$	enthalpy, Btu/lb
$h_{eff}$	effective heat of ablation, Btu/lb
$l$	length, ft
$M$	Mach number
$\dot{m}$	ablation rate, lb/ft <sup>2</sup> -sec
$N_{St}$	Stanton number
$q$	heating rate, Btu/ft <sup>2</sup> -sec
$R$	Reynolds number per foot
$r$	lateral radius of nose, ft
$r_c$	nose radius of curvature, ft

s	distance along surface, measured from stagnation point, ft
T	temperature, °F or °R as indicated
T <sub>a</sub>	temperature at which teflon ablation starts, °R
t	time, sec
V	velocity, ft/sec
ρ	density, lb/ft <sup>3</sup>
ρ <sub>c</sub>	density of teflon vapor, lb/ft <sup>3</sup>

#### Subscripts:

aw	adiabatic wall
l	local
o	initial value
sl	sea level
t	stagnation value
w	wall
∞	free-stream value

### MODEL DESCRIPTION

#### Cone

The nose cone shown in figure 1 was permanently attached to the structure of the sustainer motor by means of a magnesium insert. The nose cone was a body of revolution 12.1 inches in length, having a blunted cylinder (the nose face having a ratio of lateral nose radius to the radius of curvature equal to 1/3) and a 10° conical afterbody.

Five ablation sensors were located in the nose cone. Details of the installation are shown in figure 1. The longitudinal axes of the sensors were at right angles to the surface at each location. One sensor (sensor 2) was located at the stagnation point, whereas two others (sensors 1 and 3) were located on opposite sides of the stagnation point at  $s/r = 0.62$ . The fourth and fifth sensors were located on the 10° conical afterbody of the nose cone.

## Cylinder

Directly behind the nose cone was an inconel cylinder divided into two equal segments. A schematic diagram of the cylindrical test section is shown in figure 2. One of the segments was further divided into two equal parts, each containing an angle of  $90^\circ$ . The outer surface area of both  $90^\circ$  segments was covered with a castable polyester, one segment with a thickness of 30 mils and the other with a thickness of 10 mils. The  $180^\circ$  segment was left uncoated to serve as an inconel calorimeter. Thermocouples were located in the cylinder as shown in figure 2. The thermocouples were No. 30 gage chromel-alumel wire and were spotwelded to the inner wall of the cylinder. The thicknesses of the inconel and the polyester at the six thermocouple locations are as follows:

TABLE I.- THICKNESSES OF INCONEL AND POLYESTER

Thermocouple	Inconel thickness, in.	Polyester thickness, in.	Total thickness, in.
1	0.052	0.010	0.062
2	.053	.029	.082
3	.053	.030	.083
4	.077	0	.077
5	.052	.008	.060
6	.078	0	.078

The physical properties of the castable polyester are

Thermal conductivity, Btu/ft <sup>2</sup> -sec- $^\circ$ F/ft . . . . .	$3.61 \times 10^{-6}$
Specific heat, Btu/lb- $^\circ$ F . . . . .	0.46
Density, lb/ft <sup>3</sup> . . . . .	70
Emissivity . . . . .	0.9

## Flare

The  $10^\circ$  stabilizing flare of the third-stage sustainer motor was treated in a manner similar to that of the cylinder. However, it was only divided into two equal segments, with no further subdivisions. One-half of the surface area was covered with 100 mils of resinous material containing subliming salts. Again, the uncoated inconel segment was used as a calorimeter. The  $10^\circ$  flare is shown in figure 3. Figure 3 also shows the location of the chromel-alumel thermocouples in the flare.

## LAUNCH VEHICLE

The launch-vehicle system consisted of three stages of solid-propellant rocket motors. The first and second stages were fin-stabilized Nike rocket

motors. The third stage was a flare-stabilized Recruit rocket motor. The third-stage sustainer-rocket motor with the blunted cylinder-flare test configuration attached is shown in figure 4. The complete vehicle just prior to launching is shown in figure 5.

### Instrumentation and Telemetry

The ablation sensors are installed in the nose cone as shown in figure 1. The sensor telemeter data are obtained as a change in oscillator frequency with time. Each ablation sensor is connected in parallel with the main capacitor of the inductance oscillator circuit which determines the subcarrier oscillator frequency. As the ablation proceeds, the capacitance of the sensor decreases and the subcarrier oscillator frequency correspondingly increases. The ablated length is then computed from the subcarrier oscillator frequency. The amount of ablation expected is determined from preflight calculation, and the inductance oscillator is tuned so that its frequency range covers the maximum expected ablated length. In this manner the desired sensitivity of the sensor is obtained. A more detailed explanation of the calibration procedure is explained in reference 7.

A standard 10-channel NASA telemeter was used in telemetering the data from the model. One channel was used for each of the five ablation sensors mounted in the nose cone. However, the two sensors located on the conical afterbody of the nose cone showed erratic measurements prior to and during flight and no data from these sensors are reported. A single channel was used for telemetering the thermocouple data. The commutation rate was such that each temperature was recorded approximately five times per second. Calibrated reference voltages equivalent to 70° F, 1200° F, and 2400° F were transmitted so that the temperatures could be accurately determined. One channel was used for each of four linear accelerometers: two longitudinal, one normal, and one transverse. The longitudinal accelerometers measured the positive and negative accelerations along the major axis. The normal and transverse accelerometers measured the normal and lateral forces along the other axes of the vehicle. The trajectory and test environment of the vehicle are discussed in the following section.

### FLIGHT TEST PROCEDURE

The vehicle was ground launched at an elevation angle of 70° and along an azimuth angle of 90°. A plot of the trajectory and sequence of events is shown in figure 6. The first stage, or Nike rocket motor, burned for approximately 3.4 seconds and drag-separated immediately after burnout. The remaining two stages were allowed to coast until the desired time for second-stage ignition. The second-stage Nike was fired by a mechanical timer approximately 22.9 seconds after take-off, and burned for about 3.5 seconds. The third stage, or Recruit motor, was fired after the motor-chamber pressure fell below 175-150 lb/ft<sup>2</sup> by a pressure decay switch mounted in the head cap of the second-stage motor. At 26.4 seconds the third-stage motor ignited and burned for 1.9 seconds.

Time histories of the velocity and altitude are shown in figure 7. The solid lines were obtained from radar data, whereas the circular symbols indicate the velocity measured by the longitudinal accelerometers. The velocity obtained from the accelerometer data was used in reducing the data transmitted from the model. Fifty minutes before launch, the variations of density, temperature, and wind were measured up to an altitude of 70,000 feet. The variations of the free-stream values of density and temperature with time are shown in figure 8; also shown is the calculated variation of the stagnation temperature with time. The time histories of the free-stream Mach number and free-stream Reynolds number per foot are shown in figure 9.

The altitude at which data were obtained ranged from 27,000 feet to 76,000 feet over a Mach number range that increased from 5.00 to 8.98 and then decreased to 7.00. The corresponding range of Reynolds number per foot increased from  $11.4 \times 10^6$  to  $20.8 \times 10^6$  and then decreased to  $0.4 \times 10^6$ .

## RESULTS AND DISCUSSION

### Ablation of Nose Cone

Figure 10 presents the results of the measured ablated lengths on the nose face. Each line shown in figure 10 is the best fit that could be obtained from the measured data. The data were analyzed from 27.0 seconds to 36.0 seconds, as the ablation rates were approaching zero over the nose face.

The heating rates for the stagnation point were calculated by assuming laminar flow and using the empirical relation from reference 8, which is as follows:

$$q_t = \frac{17,600}{\sqrt{r}} \sqrt{\frac{\rho_\infty}{\rho_{sl}}} \left( \frac{V_\infty}{26,000} \right)^{3.15} \frac{H_{aw} - H_w}{H_{aw} - (H_w)_{300^\circ K}} \quad (1)$$

where the wall enthalpy  $H_w$  was computed from the specific heat  $c_{p,c}$  of teflon multiplied by the temperature of the ablating surface  $T_w$ . The heating rate reached a maximum of 420 Btu/ft<sup>2</sup>-sec at 28.7 seconds and remained above 400 Btu/ft<sup>2</sup>-sec for approximately 0.5 second. The heating rate gradually fell off until at 36.0 seconds it was about 58 Btu/ft<sup>2</sup>-sec. The heating rates as computed from equation (1) were corrected for the effects of bluntness according to figure 3 of reference 9 and are shown in figure 11. Previous experimental and analytical work has verified that the heat-transfer distribution across a surface behind a strong bow shock remains essentially constant over a wide range of Mach numbers.

A computational method for determining ablation-length changes is described in detail in reference 4. In order to facilitate the understanding and handling of the present results, only an outline of the computational procedure is



presented herein. The effective heat of ablation  $h_{eff}$  is defined as the net heat input evaluated at the temperature of the ablating surface divided by the ablation rate:

$$h_{eff} = \left( \frac{q}{\dot{m}} \right)_{\text{calculated}}$$

where the ablation rate  $\dot{m}$  is the product of the material density and the derivative of length with time (that is,  $\rho_c \frac{dl}{dt}$ ).

The theoretical  $h_{eff}$  (obtained by using actual flight data from the investigation to compute the actual enthalpy parameter) is shown in figure 11, and values of  $\dot{m}$  were computed by using the relation

$$\dot{m} = \frac{q_{\text{calculated}}}{h_{eff, \text{theory}}}$$

The procedure was repeated using the computed  $\dot{m}$  values to determine the new values of the enthalpy parameter and heat input, and is continued until the value computed for  $\dot{m}$  agrees with the value assumed at the start of the computation. Once the value of  $\dot{m}$  has been determined, the changes in ablation length with time were obtained by using the following equation:

$$l - l_0 = \frac{1}{\rho_c} \int_0^t \dot{m} dt$$

On the average, it took two iterative calculations per datum point to achieve convergence of experiment with theory. The measured ablated lengths and the ablated lengths as obtained from the analytical calculation are shown in figure 12. The agreement between the measured data and the analytical procedure (ref. 3) is excellent. The variation of the ablated-length change with time is essentially the same for the three sensors on the nose face. The stagnation-point sensor indicated an ablated-length change of 0.0833 inch, whereas sensors 1 and 3 located at  $s/r = 0.62$  showed ablated-length changes of 0.0845 inch and 0.0715 inch, respectively.

Further demonstration of the agreement between the measured data and the analytical computation is shown in figure 13, where  $h_{eff}$  is presented plotted against the enthalpy parameter

$$\left( H_{aw} - H_w \right) \frac{c_{p,c} \left( \frac{T_l}{T_w} \right)}{c_{p,l} \left( \frac{T_l}{T_w} \right)}^{0.19}$$

The excellent agreement between the measured data and the three-dimensional laminar stagnation-point case (ref. 3) further illustrates that the teflon effectiveness increased substantially with increased enthalpy difference.

### Aerodynamic Heating of Cylinder

The local heating rates over the cylinder were calculated from the following equation:

$$q = N_{St} \rho_l V_l c_p (T_{aw} - T_w)$$

where the surface temperatures were computed from measured inner-surface temperatures by using Hill's method in reference 10. The Stanton number  $N_{St}$  is taken from Van Driest (ref. 11) where it is shown as a function of the local Reynolds number, temperature, and Mach number.

The main assumptions made in this analysis are:

(1) Normal shock with isentropic expansion to free-stream pressure for determining edge-of-boundary-layer flow conditions along the cylinder

(2) All turbulent flow based on the local flow over the cylinder and a length of 0.67 foot

(3) Local Reynolds number above  $1 \times 10^6$  for the first 32.0 seconds of flight; although transition to laminar flow could be expected to occur as the Reynolds number decreases, the effect on the temperature predictions would be slight.

The comparison between the actual temperature measurements and the theoretical predictions is shown in figure 14. The predictions were calculated for effective Reynolds number lengths of 0.67 foot and 1.0 foot. It is shown that the calculated temperature curve for an effective length of 0.67 foot fits the measured data better than that calculated for an effective length of 1.0 foot. The reduction in length gives an 8-percent increase in the calculated temperatures.

Figure 15 shows the calculated aerodynamic heating rates to the uncoated inconel, based on an effective length of 0.67 foot, as well as the measured heating rates. The calculations did not account for lateral-heat-conduction effects or radiation exchange within the cylinder.

### Performance of Insulated Material on Cylinder

The computed aerodynamic heating rates in figure 15 were used to predict the inner-surface temperature-time histories for the insulated portions of the cylinder. An attempt was made to determine the best correlation between the calculated and measured temperatures as a function of the ablative properties

of the material. The insulation performance is a function of the ablative properties of the castable polyester (presented in the section entitled "Model Description"). The calculations assumed the value of  $h_{eff}$  to be independent of enthalpy (i.e., no transpiration effects) since the transpiration correction would have been negligible. The computations were performed for a 0.030-inch polyester coating on a 0.053-inch inconel section, and for a 0.010-inch polyester coating on a 0.053-inch inconel section. Table I shows slight variations from these thicknesses at several of the thermocouple stations.

An ablation program (ref. 6) was set up and the ablation rates  $\dot{m}$  and the inner-surface temperatures were computed. The ablation program was used as long as any of the ablative material remained; the Van Driest heat-transfer program (ref. 11) for turbulent flow over a flat plate was used when ablation ended. The conditions existing in the inconel at the end of the ablation program were incorporated directly into the Van Driest heat-transfer program. The ablation rates for the 10-mil insulating material indicated that essentially all the ablative material was disposed of within 28.0 seconds. In the case of the 30-mil insulating material, the ablation rates showed that ablation ceased at 29.7 seconds. An ablation temperature  $T_a$  of 1260° R and an effective heat of ablation  $h_{eff}$  of 1500 Btu/lb were used in determining the ablation rates and the inner-surface temperature. These values appear to give the best correlation with the measured data (fig. 16).

#### Stabilizing Flare

The temperature time histories obtained from the thermocouples located on the inner surface of the flare of the vehicle are shown in figure 17. Thermocouples 7 and 9 are under the resinous material. Thermocouples 8 and 10 are under the uncoated inconel section of the flare serving as a calorimeter.

A study of the data from thermocouples 7 and 9 indicates that the coating of resinous material acted primarily as a sheet of insulation with little heat-blocking effect from sublimation. It was concluded from this that few, if any, basic subliming salts were present in the coating applied to the stabilizing flare. Based on the assumption that no salts were present in the coating, the analyses of the coated area of the flare were programed as in reference 6, considering the resinous material to be acting only as an insulator, not as a sublimier. To eliminate possible errors, the heating rates used for these calculations were computed from the thermocouples located under the uncoated inconel section of the flare. These heating rates are shown in figure 18. From these heating rates and by considering the coating to be an insulator only, temperature histories were computed and are shown in figure 19. This figure indicates that some salts were present in the material which offered a minimum heat-blocking effect due to sublimation, but that after sublimation of the salts the assumption that the material acted as an insulator proved to be correct. From the analysis of results obtained from thermocouple 9 (fig. 19(b)), the reason for the decrease can be explained by observing the recorded uncoated inconel temperatures from thermocouple 10 (fig. 17(b)), noting that the temperature of the uncoated inconel section at the latter portion of the test of the low-conductivity insulation material falls off rapidly. The same heating

rate was then used to predict the performance which would have been achieved had the coating of resinous material contained adequate salts to act as a sublimer. The results of these computations are shown in figure 19.

A thorough examination of the results of the analysis leads to the conclusion that a minimum of salts was present in the resinous material applied to the flare. By considering that the material did not contain any significant amount of salts it appears to be reasonable to assume that thermostatic temperature control was not present and that the temperature data received from the flare were correct.

#### SUMMARY OF RESULTS

A three-stage rocket-propelled vehicle system was flight tested to a maximum Mach number of 8.98 to determine the ablation characteristics of several ablative materials and the heating rates over various sections of the velocity package (blunted cylinder-flare configuration). The ablated-length measurements and the thermocouple data were recorded over a Mach number range that increased from 5.00 to 8.98 and then decreased to 7.00. The corresponding range of Reynolds number per foot increased from  $11.4 \times 10^6$  to  $20.8 \times 10^6$  and then decreased to  $0.4 \times 10^6$ . The altitude variation during the test portion of the flight ranged from 27,000 feet to 76,000 feet. The investigation indicated the following results:

1. The ablated-length measurements were in close agreement with the ablated-length predictions based on the calculated heating rates and the theoretical effective heats of ablation for teflon. The effective heats of ablation for teflon, based on ablated-length measurements obtained on the nose cone and the flight conditions, were in close agreement with those predicted by the analytical method of Rashis and Hopko presented in NASA TM X-300.
2. The inconel calorimeter temperatures calculated by use of the Van Driest turbulent flow theory were in agreement with the measured temperatures over the inner surface of the uncoated inconel calorimeters, based on an effective length of 0.67 foot.
3. A combination of an ablation program and a heat-transfer program was used in correlating the data from the insulated sections of the cylinder. The computed inner-surface temperatures of the insulated cylindrical segment were in close agreement with the measured temperatures.
4. A study of the data from the resin-covered portions of the stabilizing flare indicated that the material acted as an insulator with little or no heat-blocking effect taking place due to sublimation.

Langley Research Center,  
National Aeronautics and Space Administration,  
Langley Station, Hampton, Va., April 20, 1964.

## REFERENCES

1. Rashis, Bernard, Witte, William G., and Hopko, Russell N.: Qualitative Measurements of the Effective Heats of Ablation of Several Materials in Supersonic Air Jets at Stagnation Temperatures up to 11,000° F. NACA RM L58E22, 1958.
2. Rashis, Bernard, and Walton, Thomas E., Jr.: An Experimental Investigation of Ablating Materials at Low and High Enthalpy Potentials. NASA TM X-263, 1960.
3. Rashis, Bernard, and Hopko, Russell N.: An Analytical Investigation of Ablation. NASA TM X-300, 1960.
4. Winters, Clyde W., and Witte, William G.: A Flight Investigation of Ablation on a Blunted Cylinder-Flare Configuration to a Mach Number of 8.48. NASA TN D-2354, 1964.
5. Winters, Clyde W., Witte, William G., Rashis, Bernard, and Hopko, Russell N.: A Free-Flight Investigation of Ablation of a Blunt Body to a Mach Number of 13.1. NASA TN D-1500, 1962.
6. Swann, Robert T., and Pittman, Claud M.: Numerical Analysis of Transient Response of Advanced Thermal Protection Systems for Atmospheric Entry. NASA TN D-1370, 1962.
7. Winters, Clyde W., and Bracalente, Emedio M.: A Sensor for Obtaining Ablation Rates. NASA TN D-800, 1961.
8. Detra, R. W., Kemp, N. H., and Riddell, F. R.: Addendum to "Heat Transfer to Satellite Vehicles Re-entering the Atmosphere." Jet Propulsion, vol. 27, no. 12, Dec. 1957, pp. 1256-1257.
9. Stoney, William E., Jr.: Aerodynamic Heating of Blunt Nose Shapes at Mach Numbers up to 14. NACA RM L58EO5a, 1958.
10. Hill, P. R.: A Method of Computing the Transient Temperature of Thick Walls From Arbitrary Variation of Adiabatic-Wall Temperature and Heat-Transfer Coefficient. NACA Rep. 1372, 1958. (Supersedes NACA TN 4105.)
11. Van Driest, E. R.: The Problem of Aerodynamic Heating. Aero. Eng. Rev., vol. 15, no. 10, Oct. 1956, pp. 26-41.

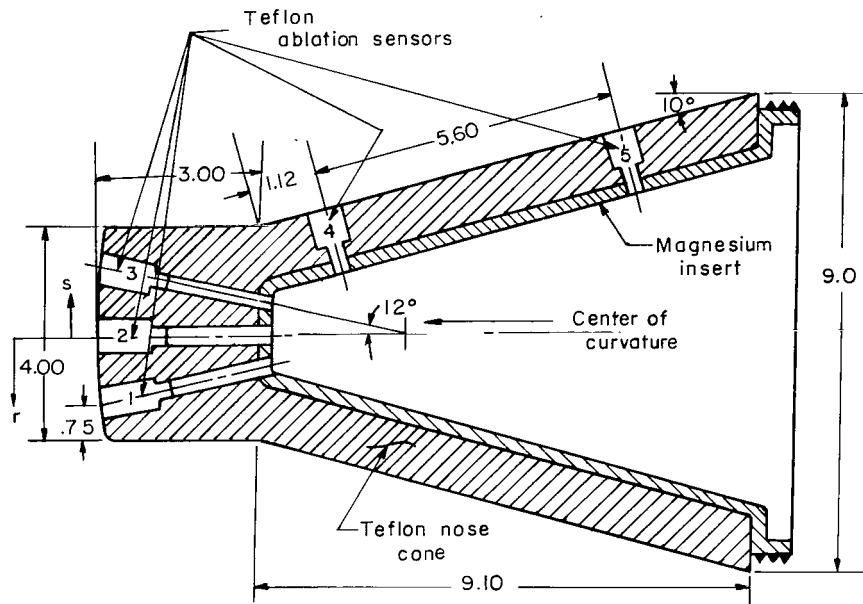


Figure 1.- Details of ablation sensor installation. All dimensions in inches.

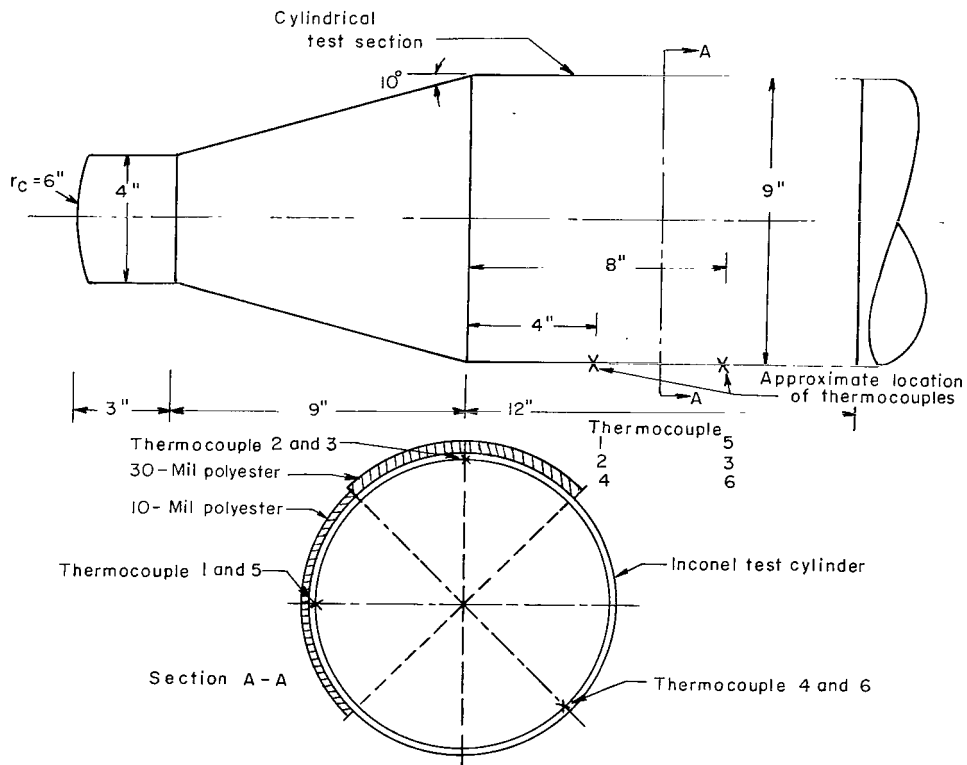


Figure 2.- Schematic diagram of nose cone and cylindrical section.

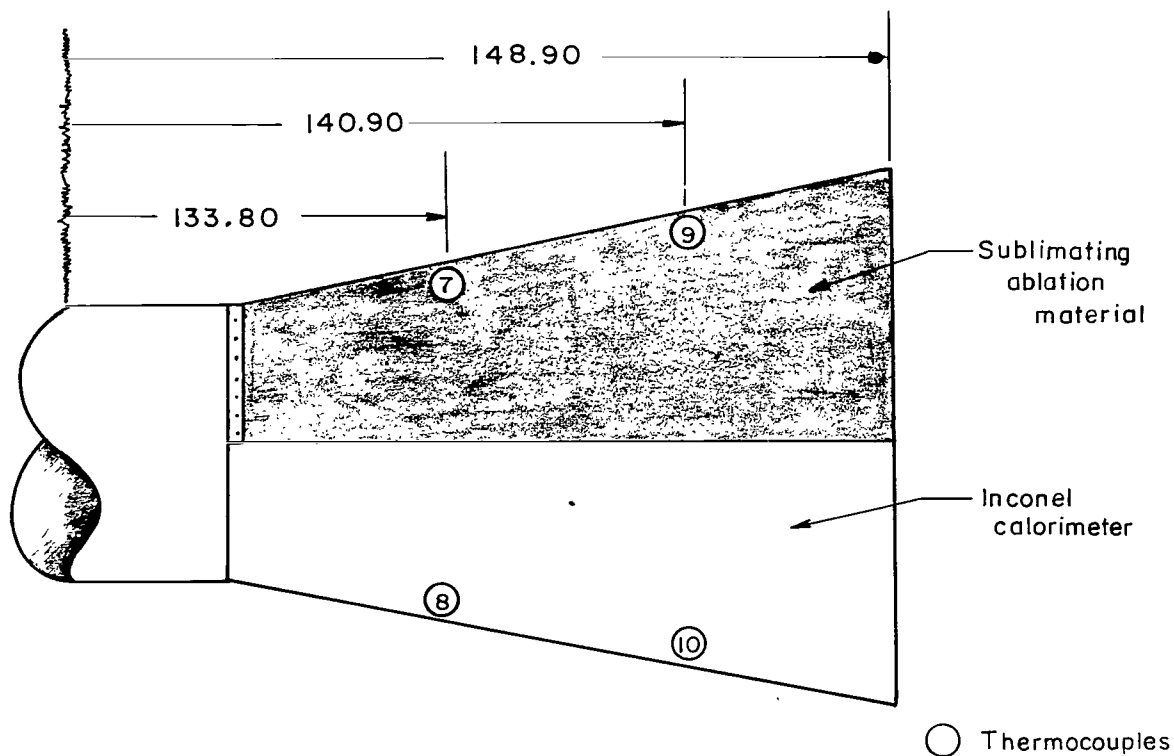


Figure 3.- Drawing of Recruit stabilizing flare. All dimensions are measured from the nose tip and are in inches.

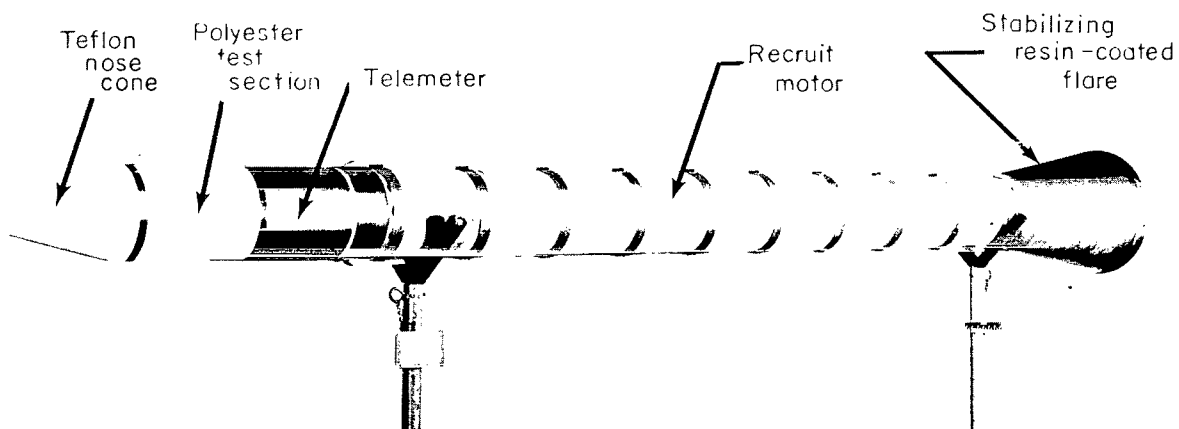


Figure 4.- Third-stage blunted cylinder-flare configuration covered with various ablative materials.

L-60-3984.2

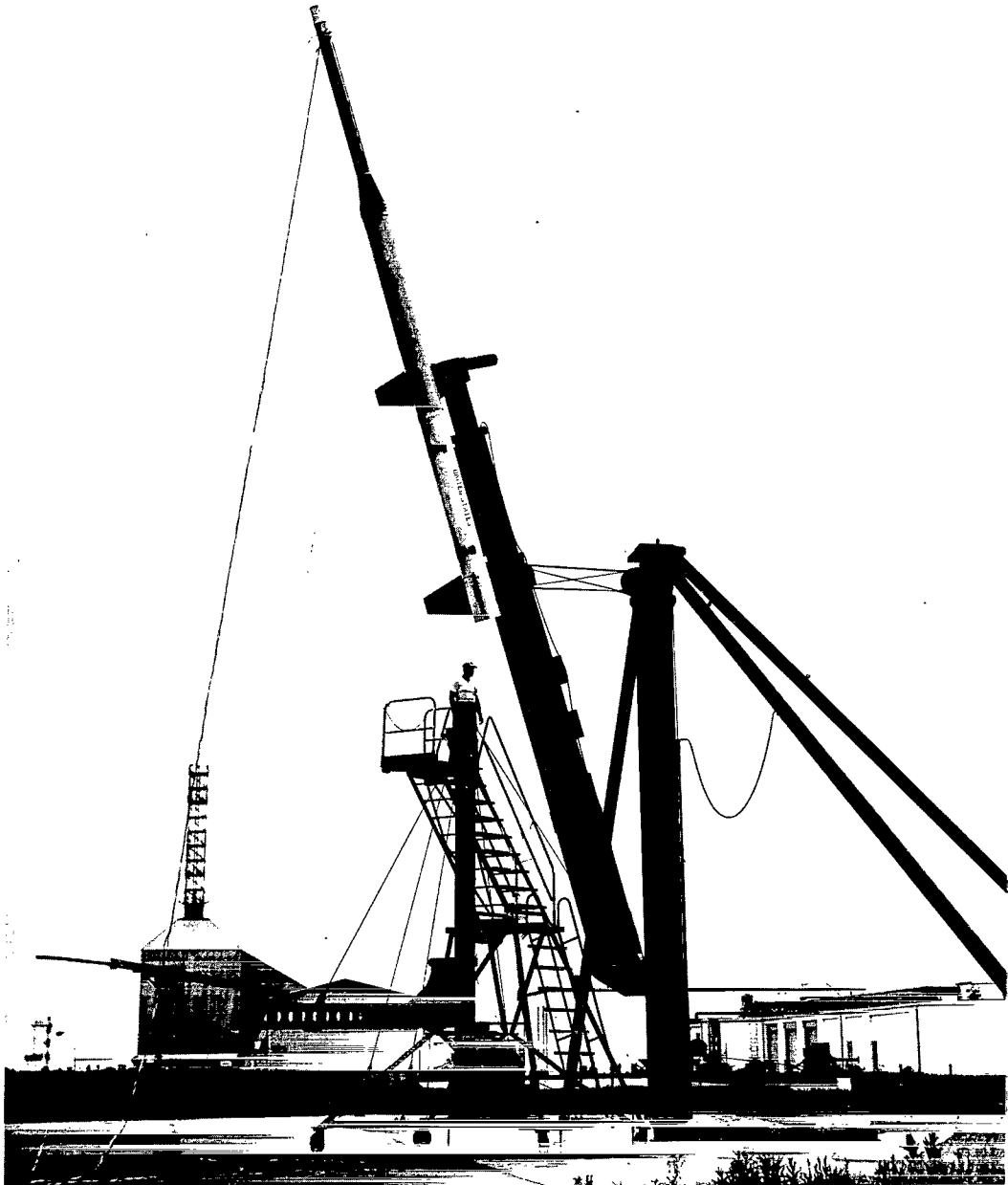


Figure 5.- Vehicle prior to launching.

L-60-5122



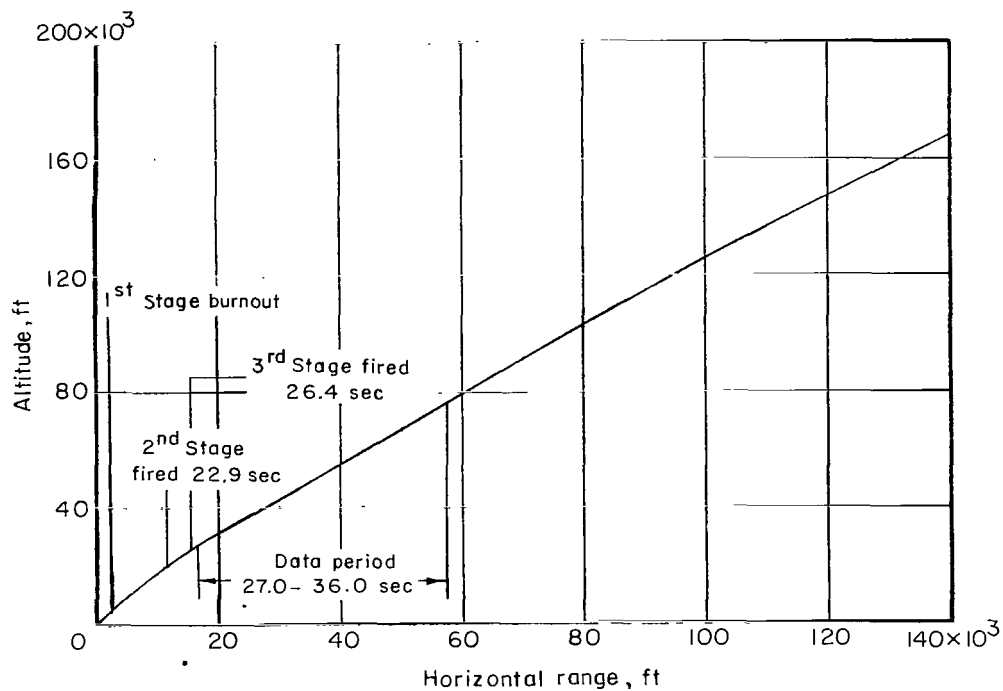


Figure 6.- Flight-trajectory altitude plotted against horizontal range.

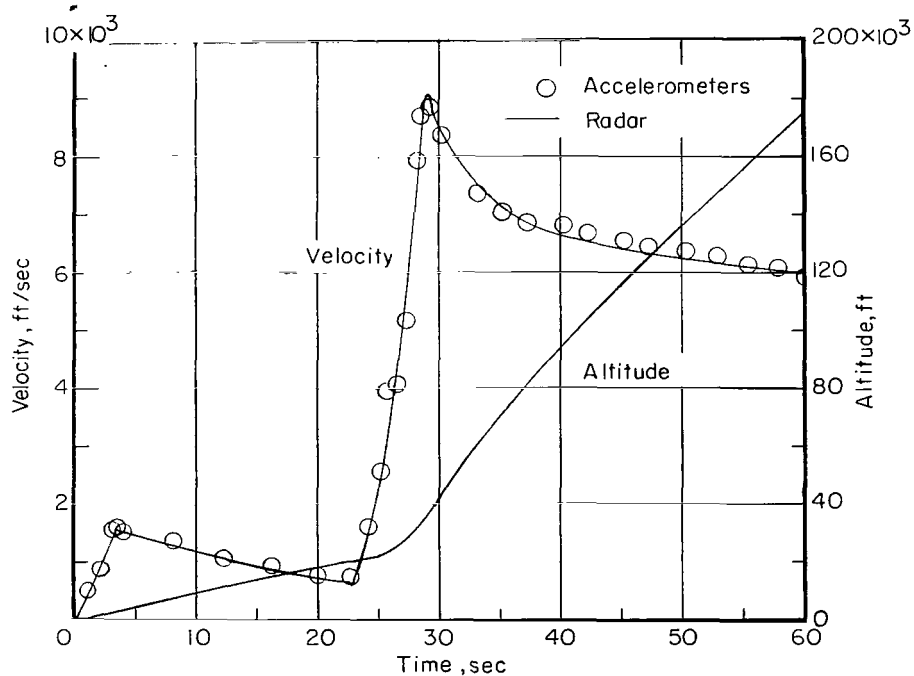


Figure 7.- Velocity and altitude for flight trajectory.

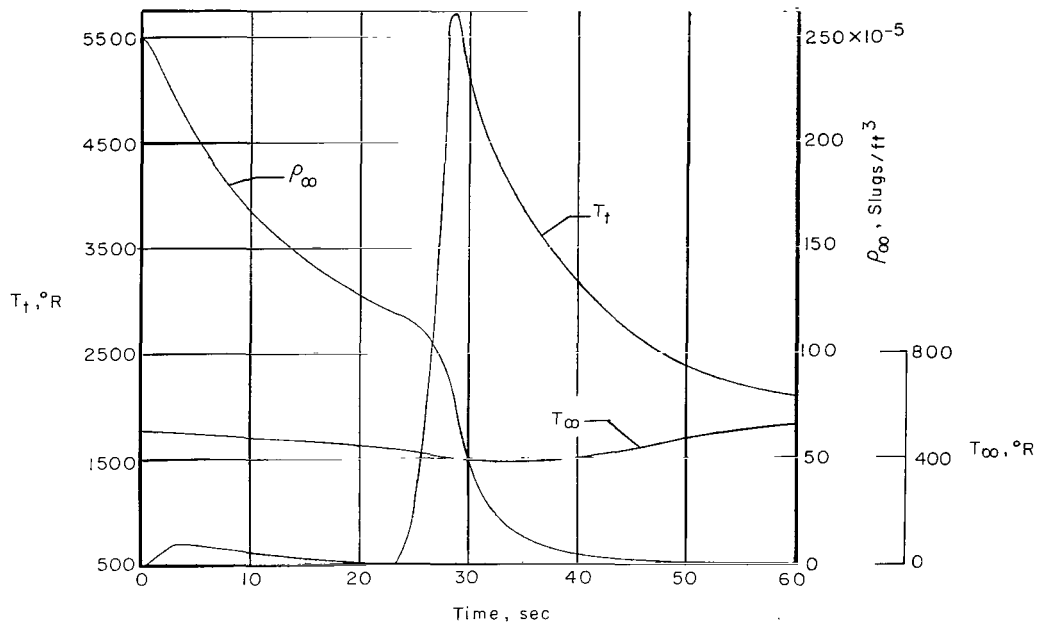


Figure 8.- Time histories of free-stream temperature and density and calculated stagnation temperature.

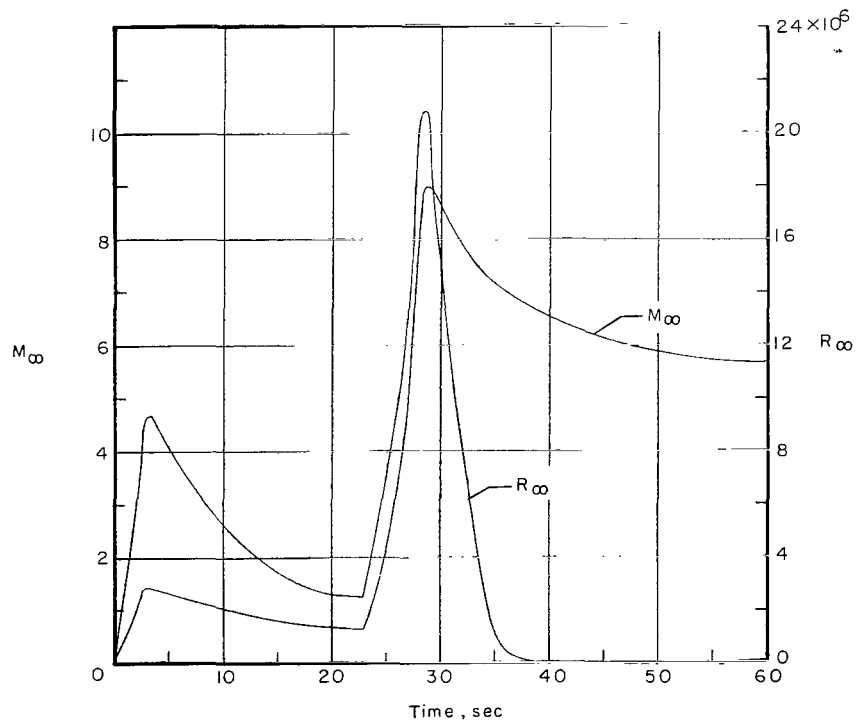


Figure 9.- Time histories of free-stream Mach number and Reynolds number.

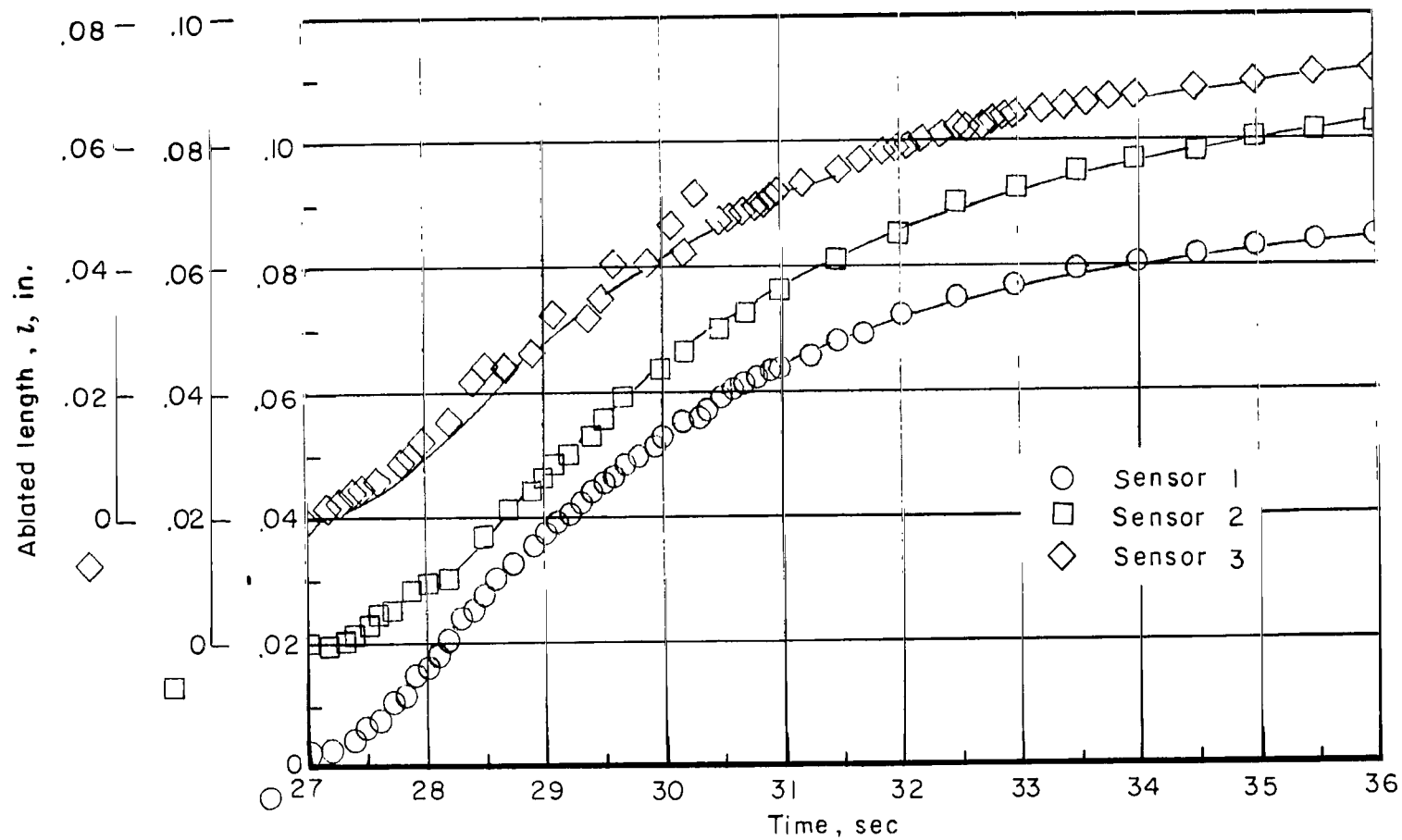
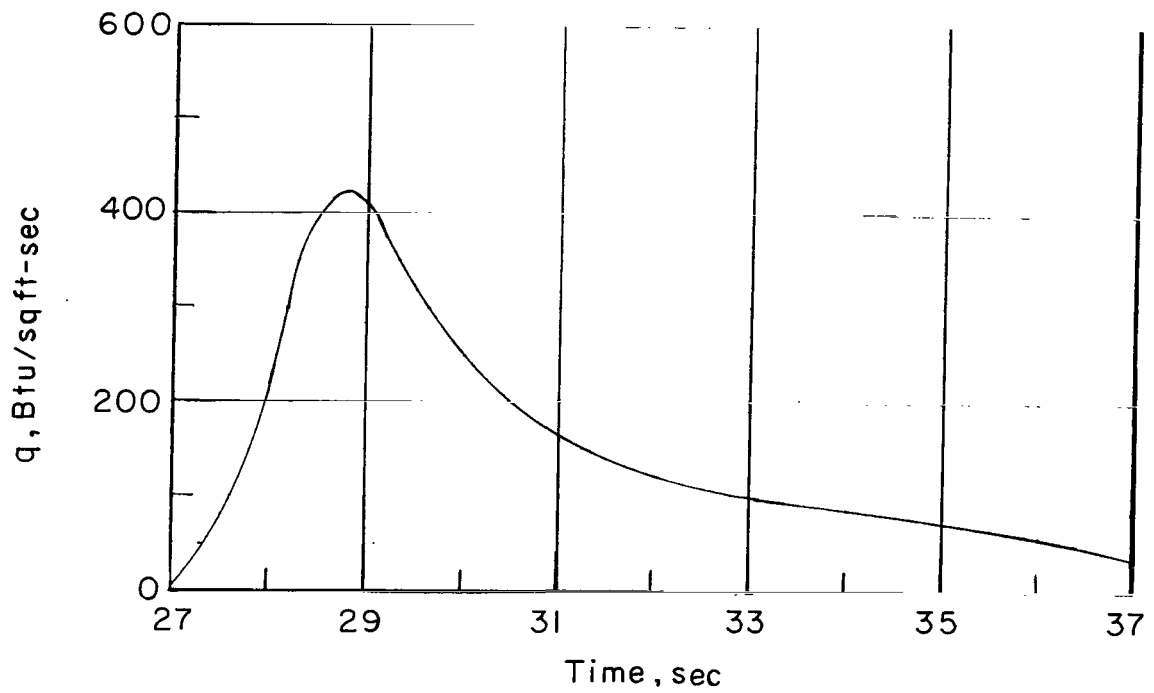
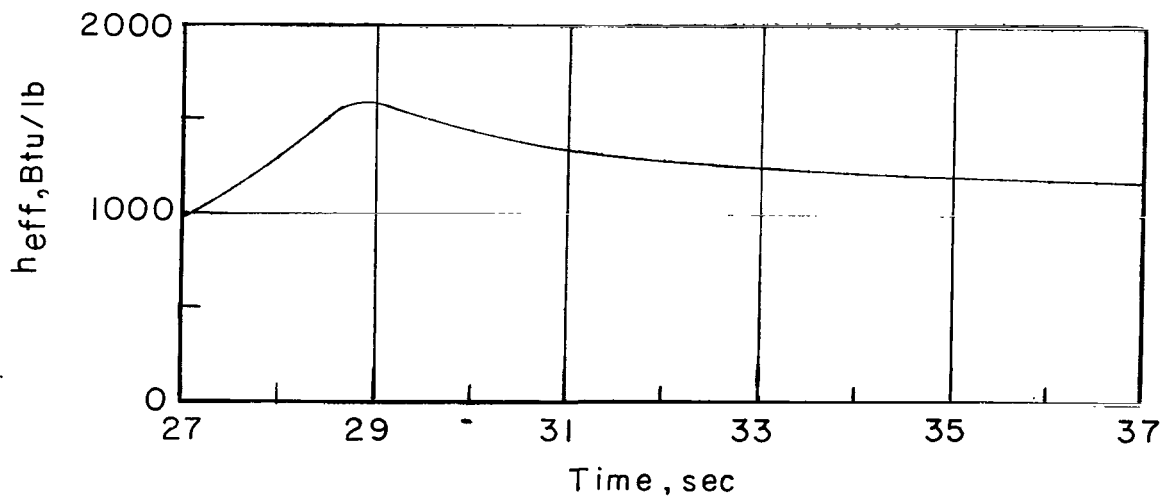


Figure 10.- Time histories of ablated lengths for sensors 1, 2, and 3.



(a) Calculated heating rates.



(b) Assumed effective heats of ablation for test.

Figure 11.- Calculated heating rates for the nose sensors and theoretical effective heats of ablation.

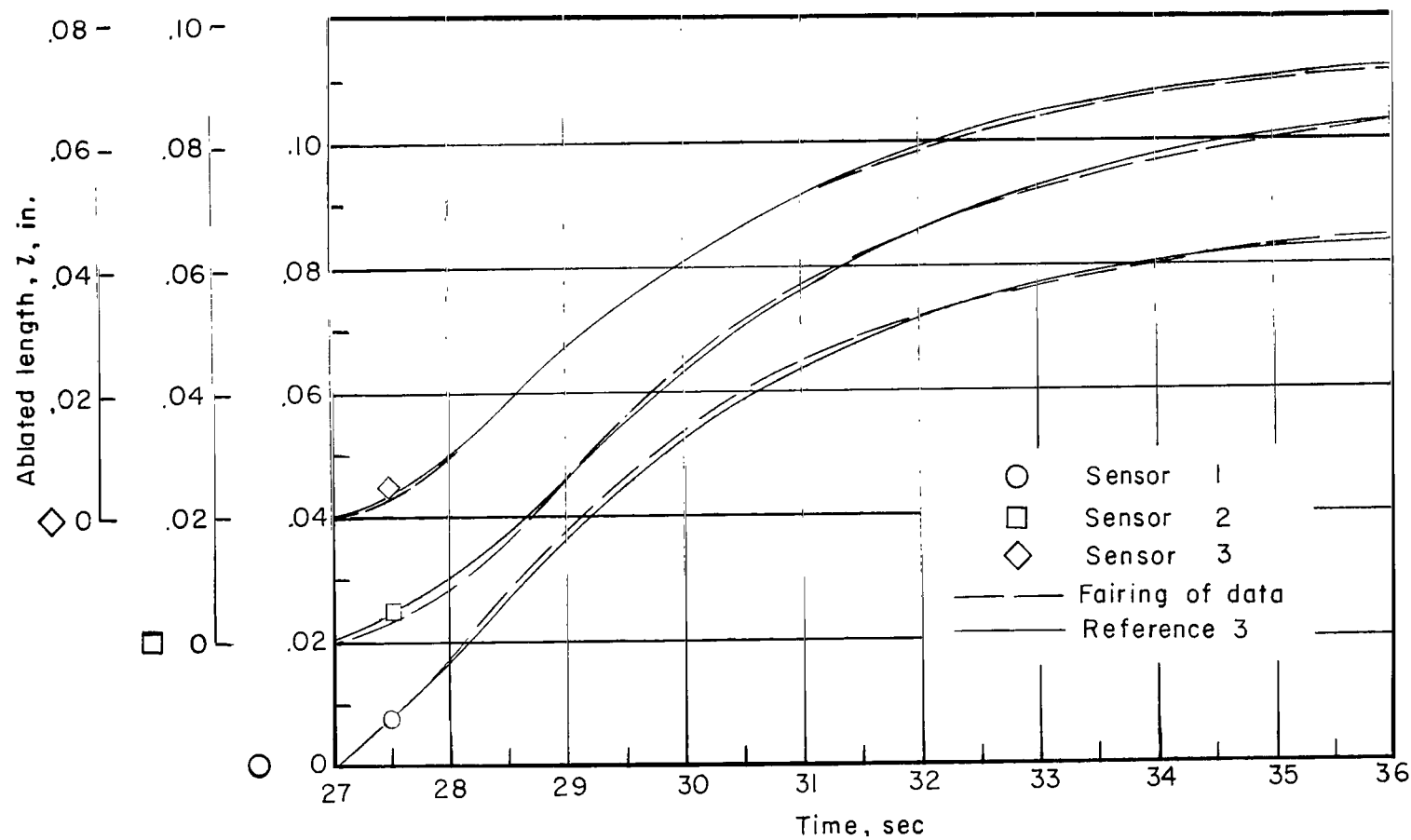


Figure 12.- Theoretical ablated lengths (ref. 3) shown with the best fairing from the measured ablated lengths.

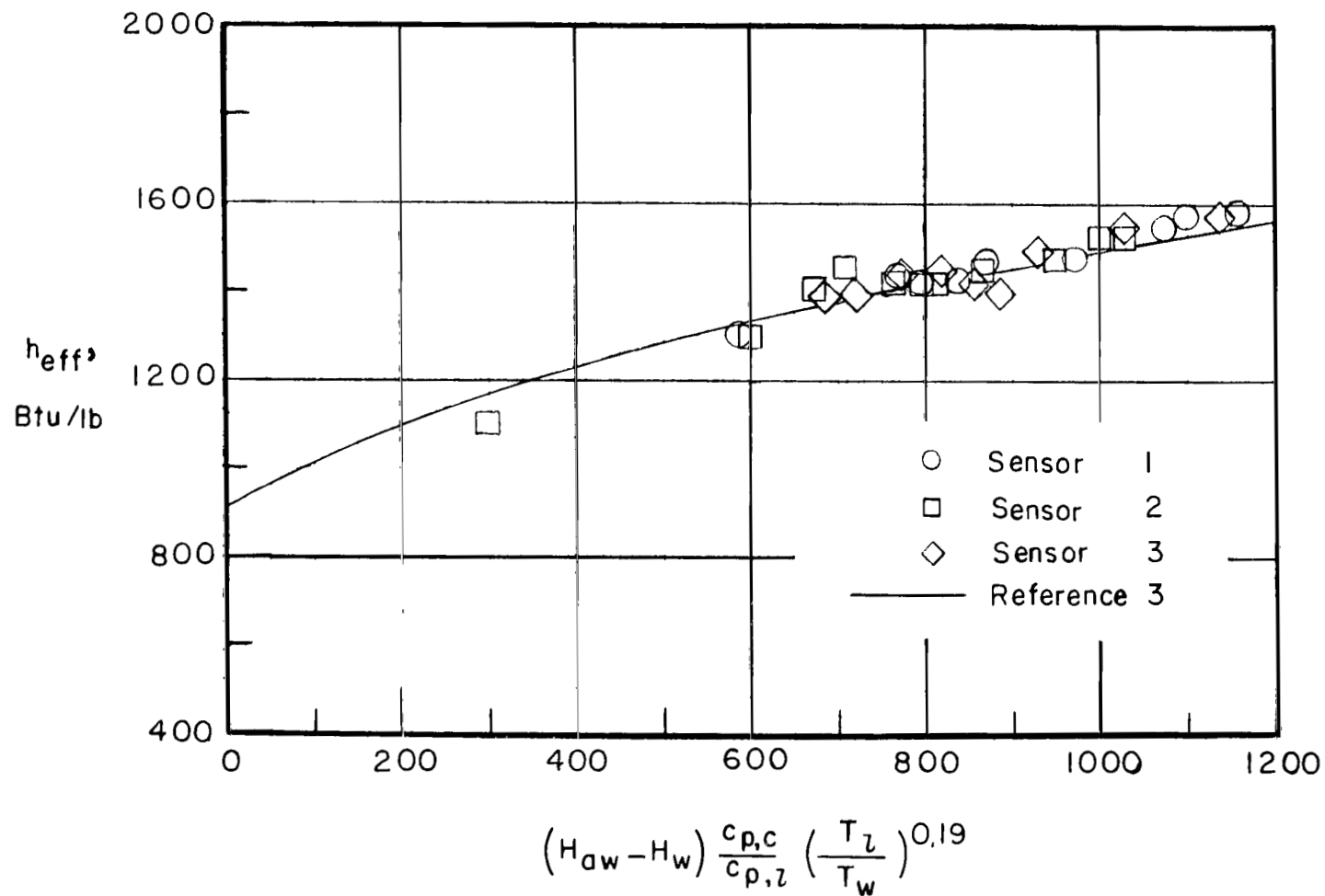


Figure 13.- Comparison of flight data with the predicted effectiveness of teflon (ref. 3).

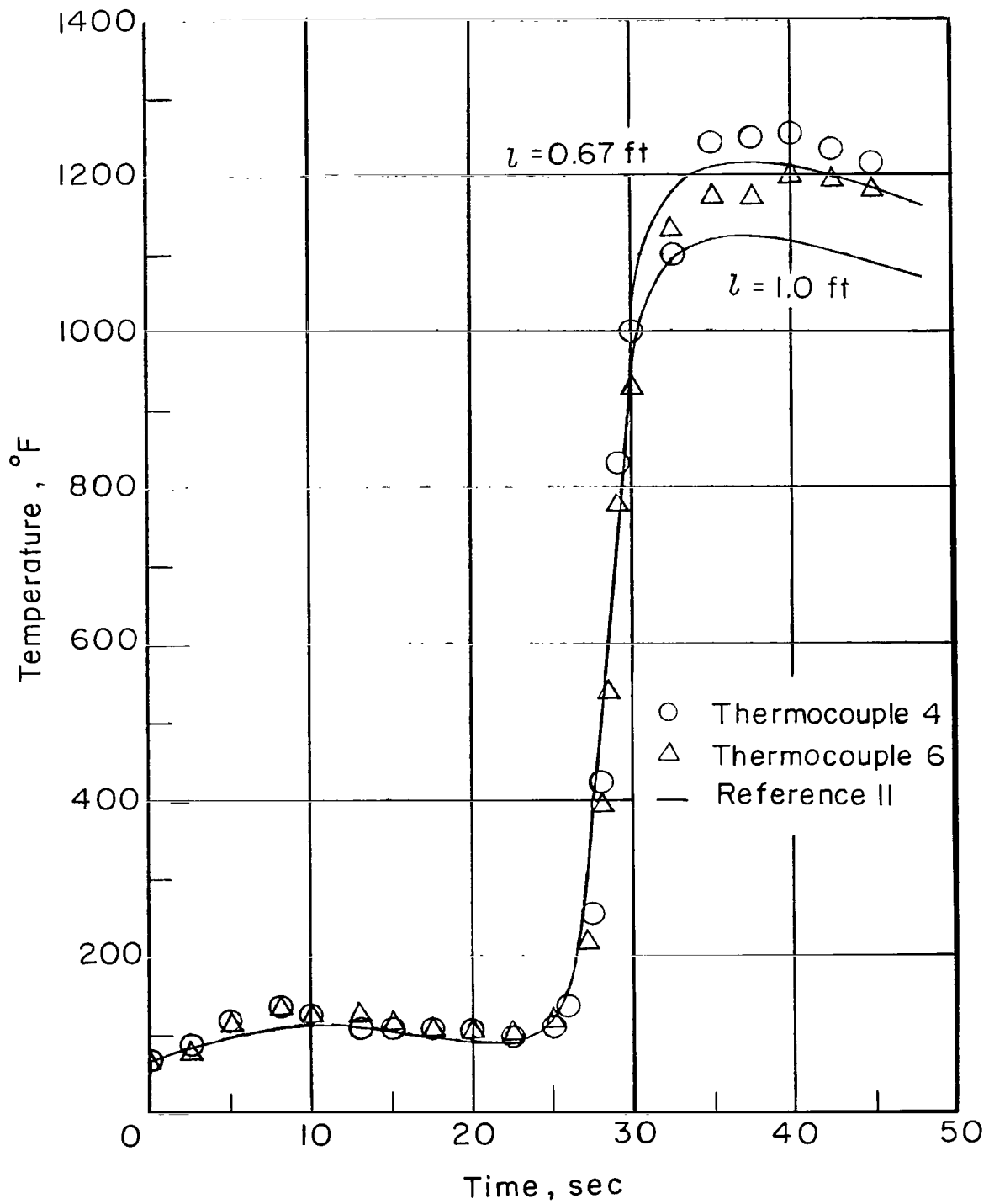


Figure 14.- Comparison of measured temperatures with the theoretical calculations (ref. 11) based on lengths of 0.67 foot and 1.0 foot.

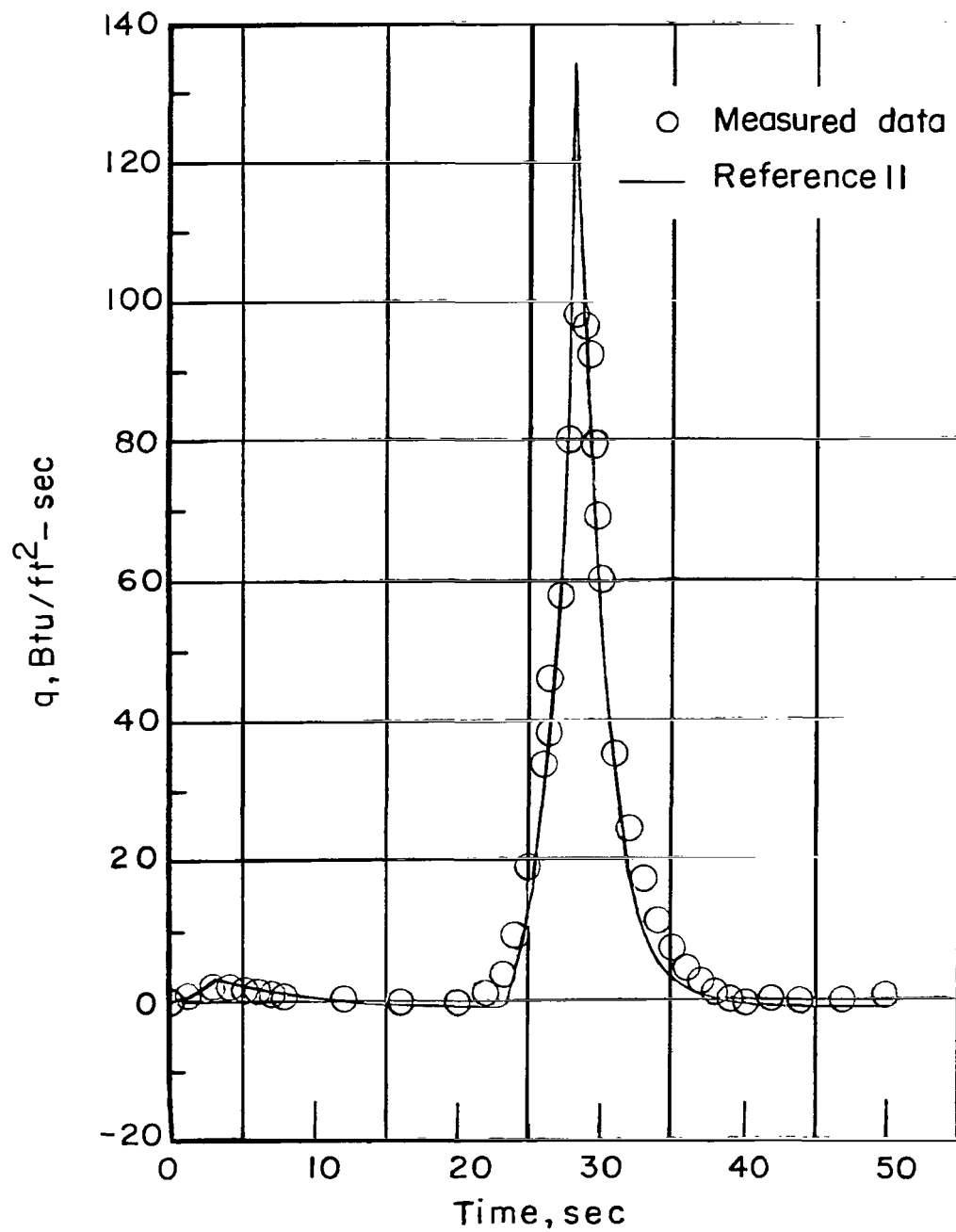
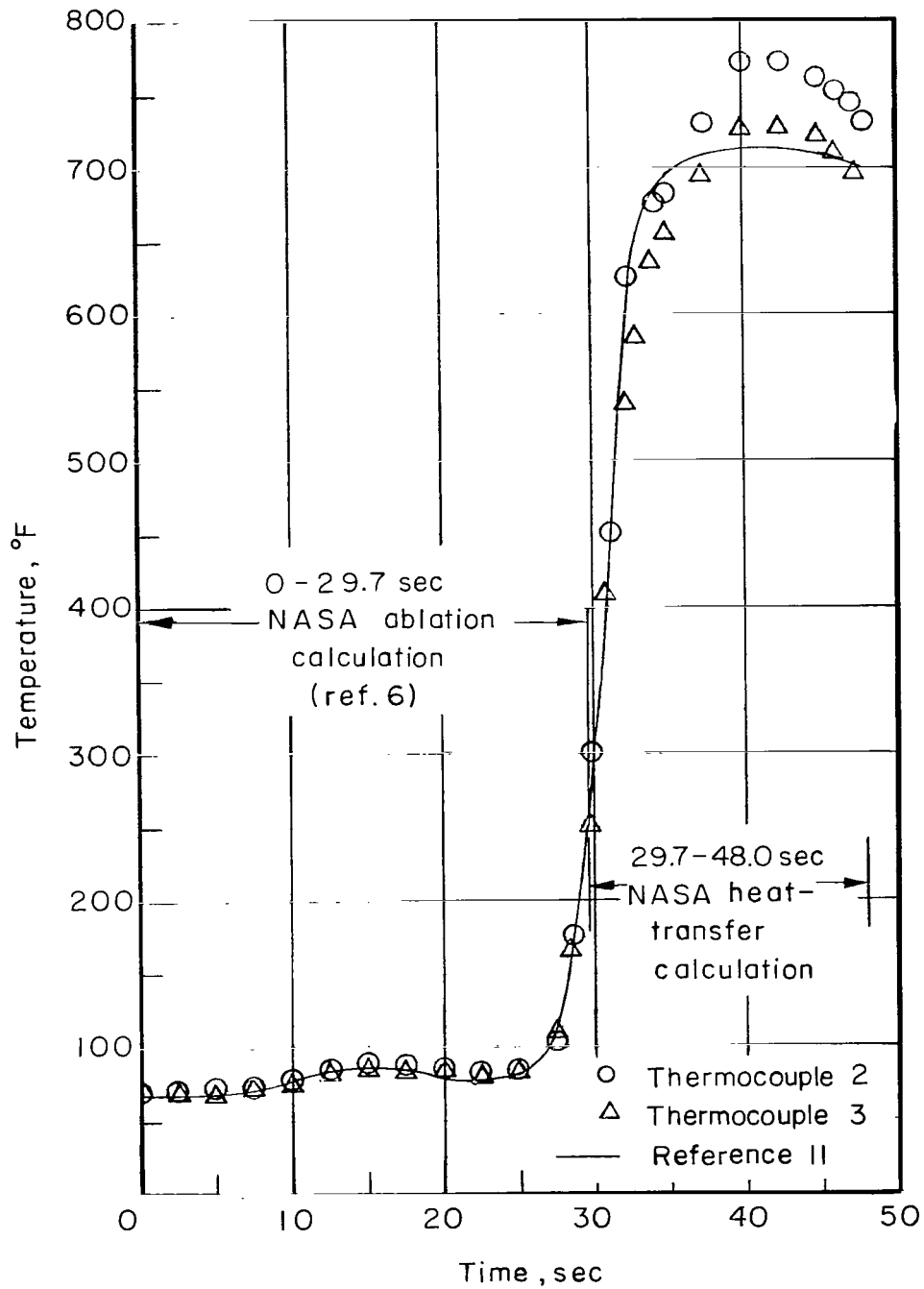


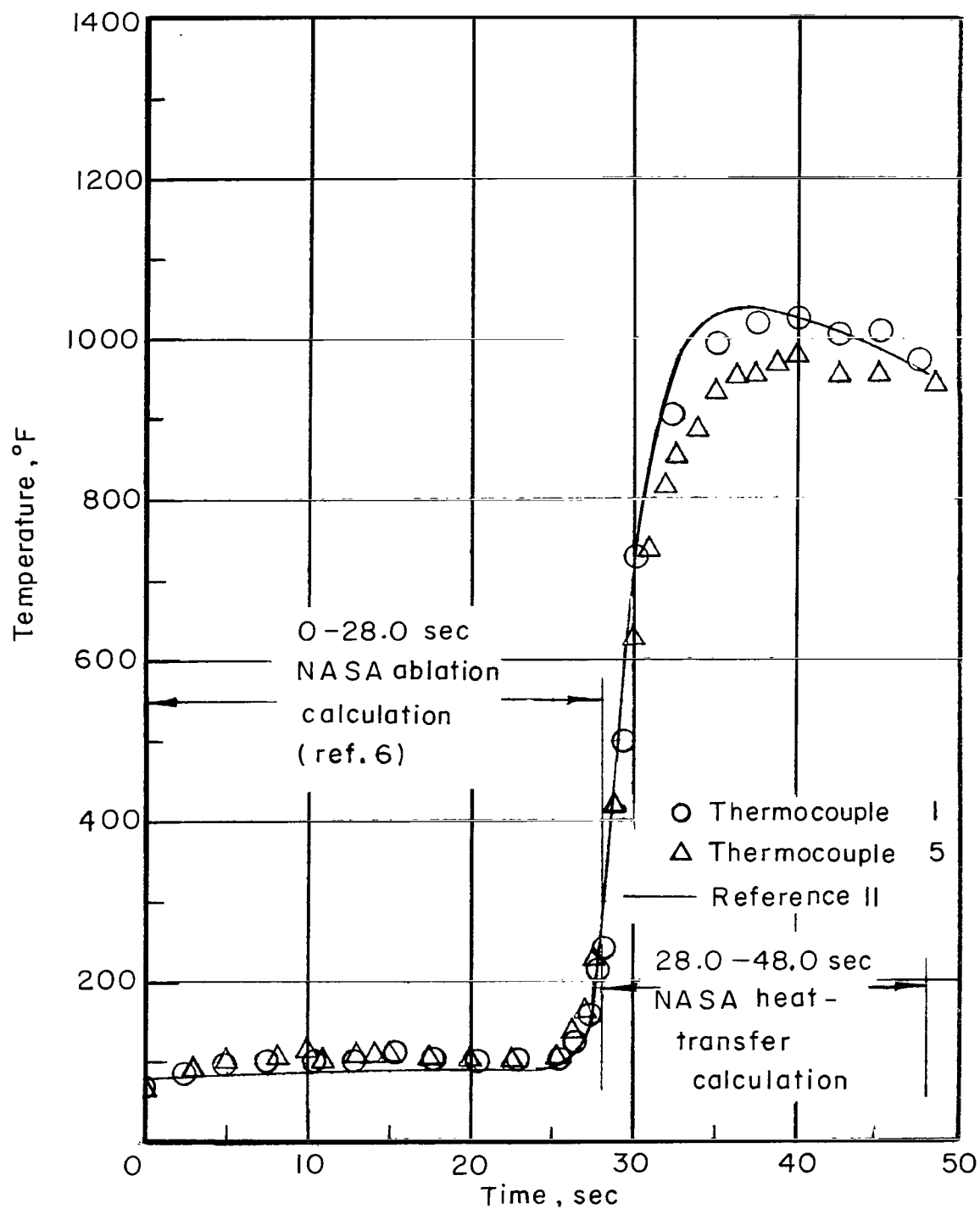
Figure 15.- Comparison of experimental heating rates with the Van Driest turbulent theory (ref. 11) over the uncoated inconel cylinder section, based on a length of 0.67 foot.





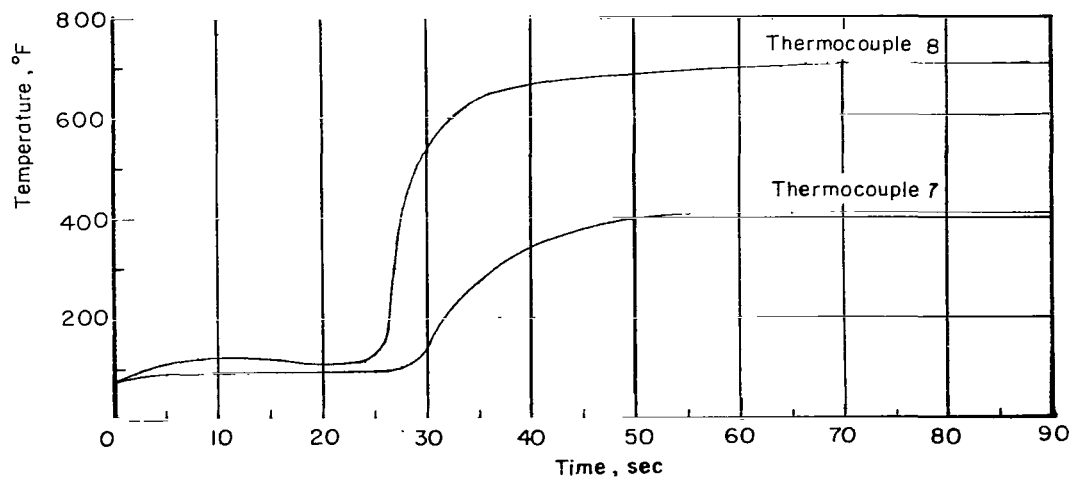
(a) 30-mil polyester.

Figure 16.- Comparison of an ablation calculation and a heat-transfer program with the measured data from thermocouples under polyester-covered cylinder.

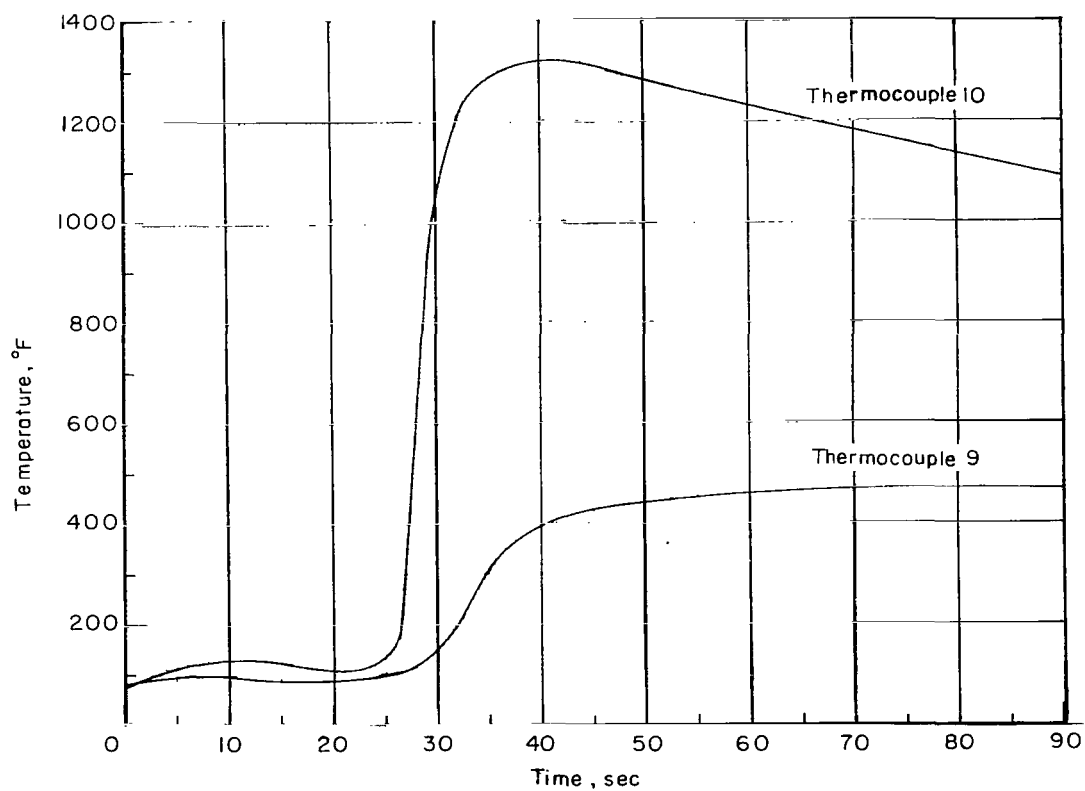


(b) 10-mil polyester.

Figure 16.- Concluded.

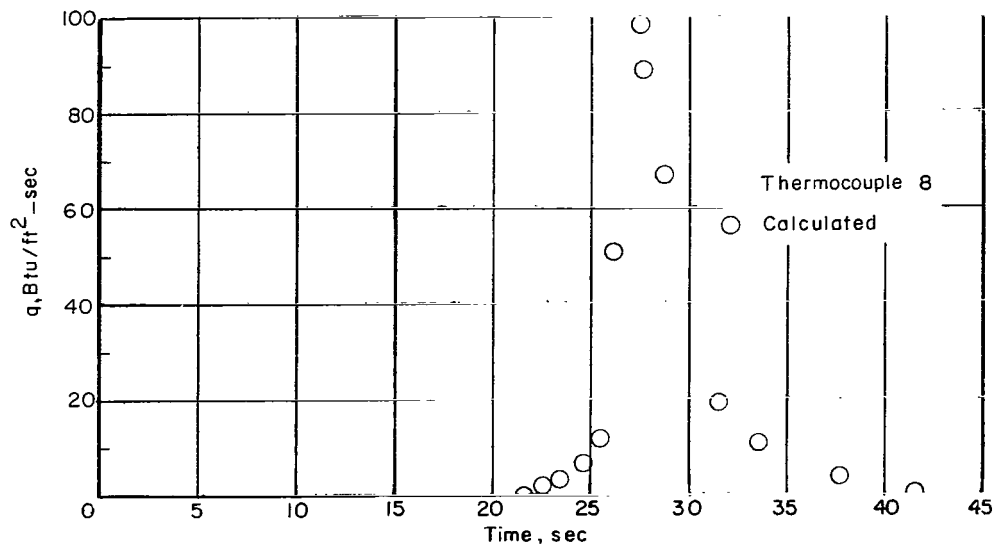


(a) 133.80 inches.

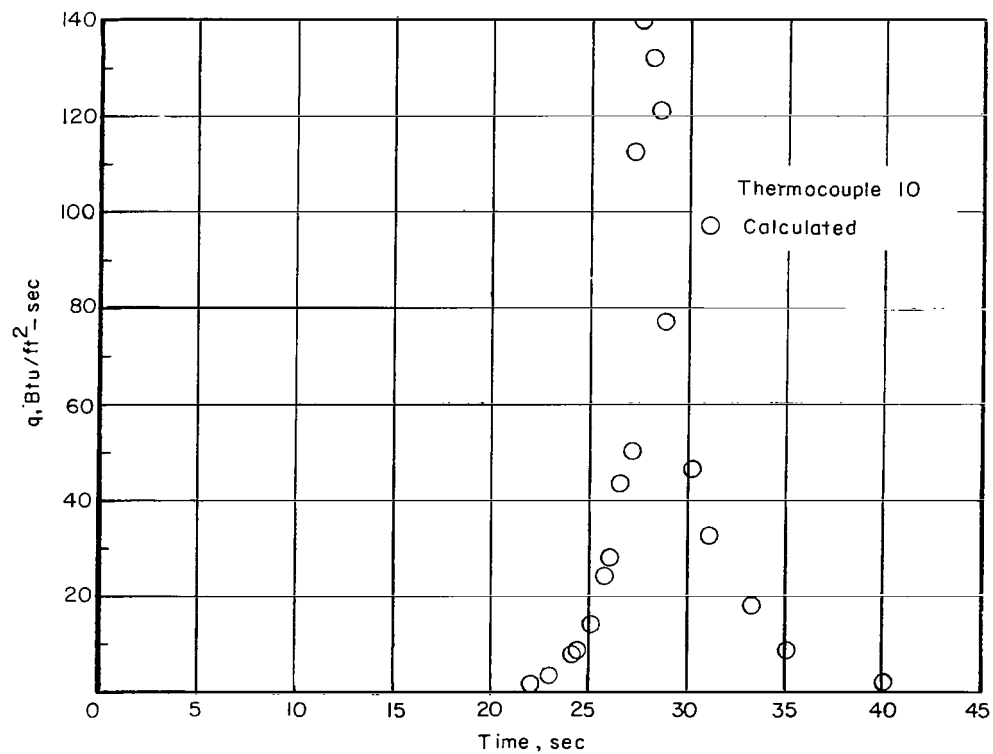


(b) 140.90 inches.

Figure 17.- Inside wall temperature along the flare.

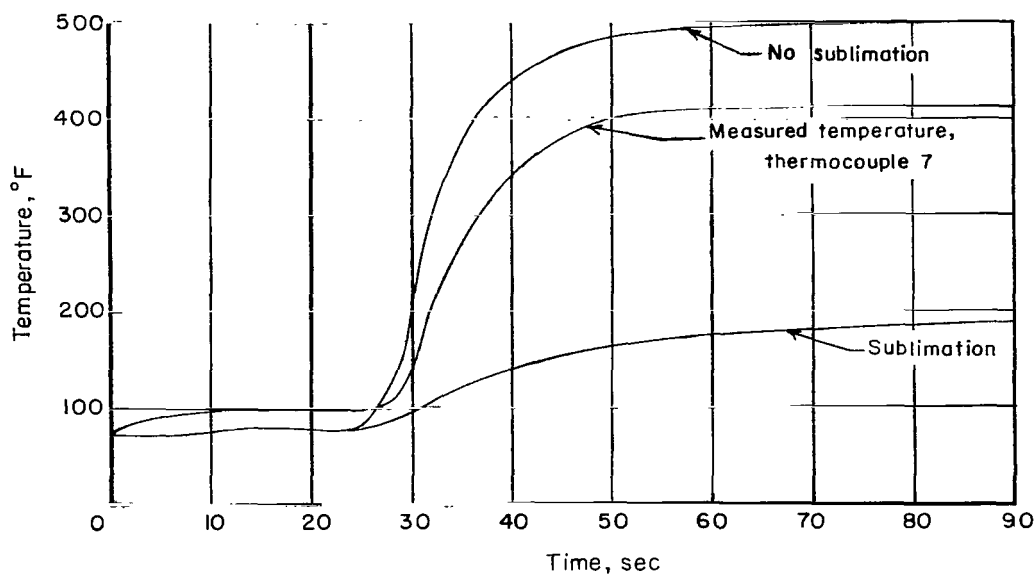


(a) 133.80 inches.

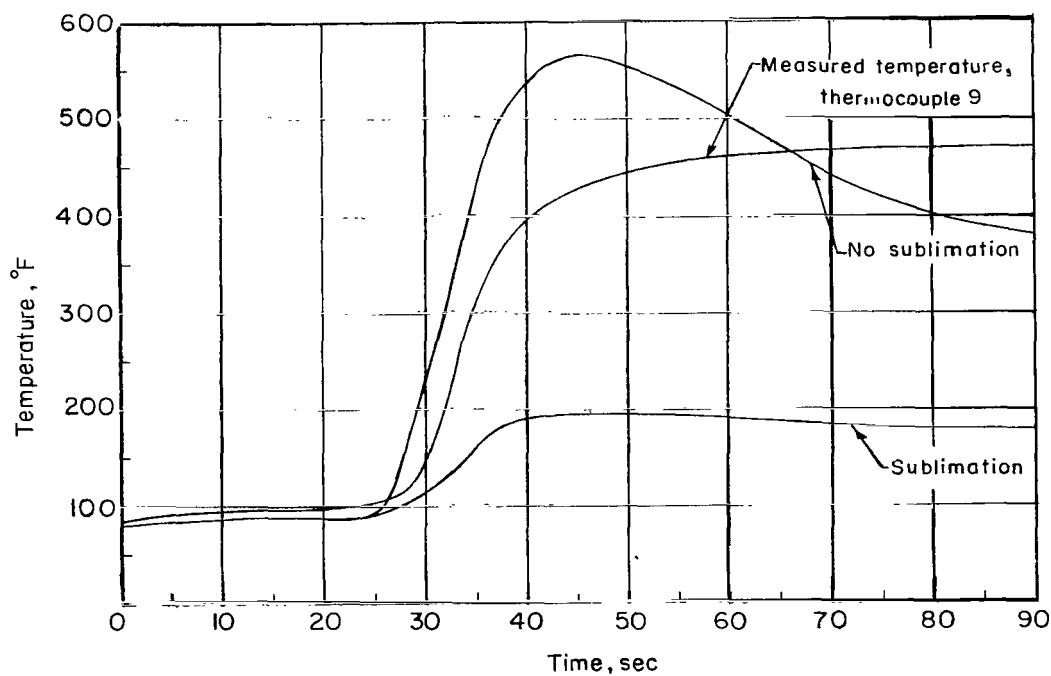


(b) 140.90 inches.

Figure 18.- Calculated heating rates for the calorimeter portion of the flare.



(a) 133.80 inches.



(b) 140.90 inches.

Figure 19.- Calculated temperatures for a sublimation and a no-sublimation case, shown with the measured wall temperatures from the stabilizing flare.

2/7/85  
3

*"The aeronautical and space activities of the United States shall be conducted so as to contribute . . . to the expansion of human knowledge of phenomena in the atmosphere and space. The Administration shall provide for the widest practicable and appropriate dissemination of information concerning its activities and the results thereof."*

—NATIONAL AERONAUTICS AND SPACE ACT OF 1958

## NASA SCIENTIFIC AND TECHNICAL PUBLICATIONS

**TECHNICAL REPORTS:** Scientific and technical information considered important, complete, and a lasting contribution to existing knowledge.

**TECHNICAL NOTES:** Information less broad in scope but nevertheless of importance as a contribution to existing knowledge.

**TECHNICAL MEMORANDUMS:** Information receiving limited distribution because of preliminary data, security classification, or other reasons.

**CONTRACTOR REPORTS:** Technical information generated in connection with a NASA contract or grant and released under NASA auspices.

**TECHNICAL TRANSLATIONS:** Information published in a foreign language considered to merit NASA distribution in English.

**TECHNICAL REPRINTS:** Information derived from NASA activities and initially published in the form of journal articles.

**SPECIAL PUBLICATIONS:** Information derived from or of value to NASA activities but not necessarily reporting the results of individual NASA-programmed scientific efforts. Publications include conference proceedings, monographs, data compilations, handbooks, sourcebooks, and special bibliographies.

*Details on the availability of these publications may be obtained from:*

SCIENTIFIC AND TECHNICAL INFORMATION DIVISION  
NATIONAL AERONAUTICS AND SPACE ADMINISTRATION  
Washington, D.C. 20546